On the design and performance of InGaN/Si double-junction photocathodes

View Online   Export Citation   CrossMark

Ishtiaque A. Navid,[1] Srinivas Vanka,[1] Rasha A. Awni,[2] Yixin Xiao,[1] Zhaoning Song,[2] Yanfa Yan,[2] and Zetian Mi[1,a)]

AFFILIATIONS

[1]Department of Electrical Engineering and Computer Science, University of Michigan, Ann Arbor, 1301 Beal Avenue, Ann Arbor, Michigan 48109, USA
[2]Department of Physics and Astronomy, and Wright Center for Photovoltaics Innovation and Commercialization (PVIC), University of Toledo, Toledo, Ohio 43606, USA

Note: This paper is part of the APL Special Collection on Materials for Renewable Fuels Production.
a)Author to whom correspondence should be addressed: ztmi@umich.edu. Telephone: 1-734-764-3963.

ABSTRACT

Through a combined theoretical and experimental study, we have investigated the synthesis and performance characteristics of InGaN/Si double-junction photoelectrochemical (PEC) water splitting devices, which promise a theoretical solar-to-hydrogen conversion efficiency $\sim$30% under AM 1.5G one-sun illumination. The double-junction photocathodes consist of a p^+-InGaN top light absorber and a Si bottom p-n junction, which are connected through a nanowire tunnel junction. The effect of indium composition of the top light absorber as well as the impact of p-type Mg dopant incorporation on the PEC performance was studied. Experimentally, the sample with 32% indium composition showed a maximum photocurrent density of $\sim$9 mA/cm^2 at 0.4 V vs reverse hydrogen electrode (RHE) with applied bias photon-to-current efficiency (ABPE) of $\sim$9.5%. An optimum p-type doping level $\sim$1 × 10^{17} cm^{-3} was also identified, which results in the best device performance as a result of optimum surface band bending as well as vertical charge carrier (hole) transport. These results also show a good agreement with our theoretical analysis. This work provides significant insights in advancing the design and development of high efficiency PEC devices for artificial photosynthesis using industry ready materials, e.g., Si and GaN, to achieve large-scale, low-cost onsite hydrogen fuel production.

Published under an exclusive license by AIP Publishing. https://doi.org/10.1063/5.0050708

Photoelectrochemical (PEC) water splitting utilizing solar energy has emerged as one of the most promising means of hydrogen production with renewable energy resources. Since the initial demonstration of PEC water splitting using an n-TiO$_2$ electrode in 1972,[1] extensive efforts have been devoted to the creation of an efficient and stable photoelectrode but with limited success.[2–4] Studies have suggested that a double-junction PEC device, consisting of a top and bottom cell with energy bandgap $\sim$1.8 eV and $\sim$1.1 eV, respectively, can exhibit solar-to-hydrogen conversion efficiency up to $\sim$30%.[5–9] To date, most of the reported high efficiency tandem PEC water splitting devices are based on III–V compound semiconductors, e.g., III–arsenides and phosphides,[10–12] which, however, suffer from poor stability due to photocorrosion in alkaline or acidic electrolytes.[13,14] In addition, their practical application has been limited by the high cost associated with III–V substrates.[15] Recent studies have shown that Si and Ga(In)N, the two most produced semiconductors, are practically suited for

double-junction PEC devices.[16,17] With an energy bandgap of 1.1 eV, Si is ideal for the bottom light absorber, whereas Ga(In)N exhibits a tunable direct energy bandgap from 3.4 eV for GaN to $\sim$0.65 eV for InN.[18] In$_{0.5}$Ga$_{0.5}$N can exhibit a direct energy bandgap of $\sim$1.75 eV and is suited for the top light absorber.[5] Moreover, studies suggested that the conduction band edge of GaN is near-perfectly aligned with that of Si, allowing for the efficient charge carrier (electron) transport across the heterointerface.[19] To date, however, the realization of high quality InGaN epilayers directly on Si substrate has remained extremely challenging, due to the large lattice mismatch and the resulting large densities of defects and dislocations. The PEC device performance is also limited by the surface recombination of photogenerated carriers[20,21] and weak adhesion of photocatalyst nanoparticles on the device surface.[22,23] Moreover, an electrically conductive, optically transparent tunnel junction with low structural defects is essentially required for such a tandem photoelectrode.[24] Recent studies have

shown that high quality InGaN nanostructures can be grown directly on Si substrate.[25–28] Moreover, GaN nanostructures synthesized under N-rich conditions can exhibit N-termination,[19,29] not only for their top c-plane, but also for their nonpolar sidewalls, which, together with the formation of oxynitrides, can protect against photocorrosion and oxidation.[30–33] To date, however, there have been few studies on the functionality, design, and synthesis of double-junction photoelectrodes, consisting of a planar bottom light absorber and one-dimensional nanowire top light absorber.[34]

In this study, we have performed a detailed investigation of the design and performance characterization of InGaN/Si double-junction photocathodes. Theoretically, we have calculated the device performance and analyzed its dependence on the energy bandgap, p-type doing, and surface and bulk recombination of the top light absorber. Experimentally, we have synthesized and studied such unique double-junction PEC devices and further examined the impact of energy bandgap of InGaN top light absorber as well as p-type Mg-dopant incorporation in the InGaN light absorbing region, which showed good agreement with theory. The sample with ~32% indium composition showed a maximum photocurrent density of ~9 mA/cm^2 at 0.4 V vs reverse hydrogen electrode (RHE) with applied bias photon-to-current efficiency (ABPE) of ~9.5%. An optimum p-type concentration ~1×10^{17} cm^{-3} was also identified, which results in the best device performance because of optimum surface band bending as well as vertical charge carrier transport. These studies provide critical insight on the design and development of next generation PEC water splitting devices that are relevant for large-scale solar hydrogen fuel production.

The design of InGaN/Si double-junction photocathode is schematically shown in Fig. 1(a), which consists of a p-InGaN nanowire top light absorber and a planar n$^+$-p Si bottom junction. The top and bottom light absorbers are connected through a p^{++}-InGaN/n^{++}-InGaN nanowire tunnel junction.[34] In this design, photogenerated electrons are extracted from n$^+$-p Si junction by n$^+$-InGaN nanowires, which subsequently recombine with photogenerated holes of the top p$^+$-InGaN segment in the tunnel junction.[28,35–39] The bottom n$^+$-InGaN layer also functions as an active hole-blocking segment for n$^+$-p Si junction. Photogenerated electrons in the top InGaN nanowires, on the other hand, migrate to the lateral surfaces and drive proton reduction. Figure 1(b) depicts the energy band diagram of the tandem structure under light illumination. Due to the downward surface band bending, photogenerated electrons in the top p$^+$-InGaN segment can be readily extracted and migrated to the semiconductor/electrolyte interface to drive proton reduction. Shown in Fig. 1(c) are the calculated J–V curves for the p^+-InGaN/TJ/n^+-InGaN nanowires/n$^+$-p Si photocathode with various indium compositions. A maximum photocurrent density of ~18 mA/cm^2 is obtained for an In$_{0.46}$Ga$_{0.54}$N top junction (E$_g$ ~1.8 eV) under AM 1.5G illumination in the ideal case (see supplementary material Table S2). However, it is still very challenging to realize the growth of high crystalline quality InGaN nanowires with a high indium concentration, such as 46%, due to phase segregation and defect formation.[28,39] Thus, experimental demonstration of the tandem device with 46% indium will require more work in the future. In practice, the presence of surface recombination and bulk defects and the reduced indium incorporation in the top light absorber may also limit the device performance. Taking these factors into account, the maximum photocurrent density was calculated to be

~6.5 mA/cm^2 and 9.2 mA/cm^2 for InGaN top junctions with indium compositions of 26% and 32%, respectively. Perfect light absorption is assumed in these calculations based on previous studies[19,40,41] but may deviate from practical experimental conditions depending on the design and synthesis of InGaN nanowires. A detailed calculation of variations of the maximum photocurrent density, i.e., short circuit current density J$_{sc}$, vs energy bandgap and thickness of the top InGaN junction is further shown in Fig. 1(d). Due to the direct energy bandgap and large absorption coefficient of InGaN, a thickness of ~0.5 μm can absorb most of the photons with energy above the bandgap. Enhanced light absorption is further expected due to the light trapping effect of InGaN nanowire arrays.

Experimentally, the n$^+$-p Si junction was first fabricated using thermal diffusion process. Subsequently, InGaN tunnel junction nanowires were grown using a Veeco Gen II molecular beam epitaxy (MBE) system equipped with a radio frequency plasma-assisted nitrogen source. The nanowires were grown under nitrogen-rich conditions to promote the formation of N-terminated surfaces to protect against photocorrosion and oxidation.[31] Details of the growth conditions can be found in the supplementary material and in previous publications.[30,34,42] Herein, a detailed understanding of growth parameters has particularly been focused for analyzing the impact of In composition as well as Mg doping on the device performance. Extensive MBE growth was performed for such analysis, including a broad range of studies on variations of the design and growth parameters. The samples shown here are based on our detailed, in-depth studies of the epitaxy, materials characterization, and device testing. Figure 2(a) shows the normalized photoluminescence (PL) spectra for p$^+$-InGaN/tunnel junction/n$^+$-InGaN nanowires on n$^+$-p Si measured at room temperature. Here, the emission peaks correspond to average indium compositions of 26% and 32%, respectively.[34] The SEM image is shown in Fig. 2(b). The nanowires are vertically aligned on n$^+$-p Si wafer, with diameters ~90 nm and lengths ~850 nm. Through extensive growth optimizations, it has been identified that the optimum thickness for the top p$^+$-InGaN is ~500 nm to absorb most of the photons above the energy bandgap without significantly compromising the vertical transport of photogenerated holes. Pt nanoparticles were deposited on p$^+$-InGaN/TJ/n$^+$-InGaN nanowires by photodeposition. Our previous studies have demonstrated that Pt nanoparticles are uniformly distributed on the nanowire surfaces to promote proton reduction.[43]

Figure 3(a) presents the three-electrode linear scan voltammograms (LSV) of the InGaN/Si double-junction photocathodes in 0.5 M H$_2$SO$_4$ under AM 1.5G one-sun illumination for indium compositions of 26% and 32%, showing an onset potential of ~2 V vs RHE. For comparison, the performance of a single-junction GaN/Si photocathode is also shown, which exhibits an onset potential ~0.52 V vs RHE. The significantly increased onset potential clearly illustrates the role of the top junction. A detailed comparison of the open circuit potential (OCP) measurements between single-junction InGaN and double-junction InGaN/Si further confirmed the operation of the double-junction device (see supplementary material Fig. S1). It is also seen that the photocurrent density increases with increasing indium incorporation in the top junction, due to the smaller energy bandgap and more efficient sunlight absorption. For the device with the In$_{0.32}$Ga$_{0.68}$N top junction, a maximum photocurrent density ~9 mA/cm^2 at 0.4 V vs RHE was measured. ABPE values of these
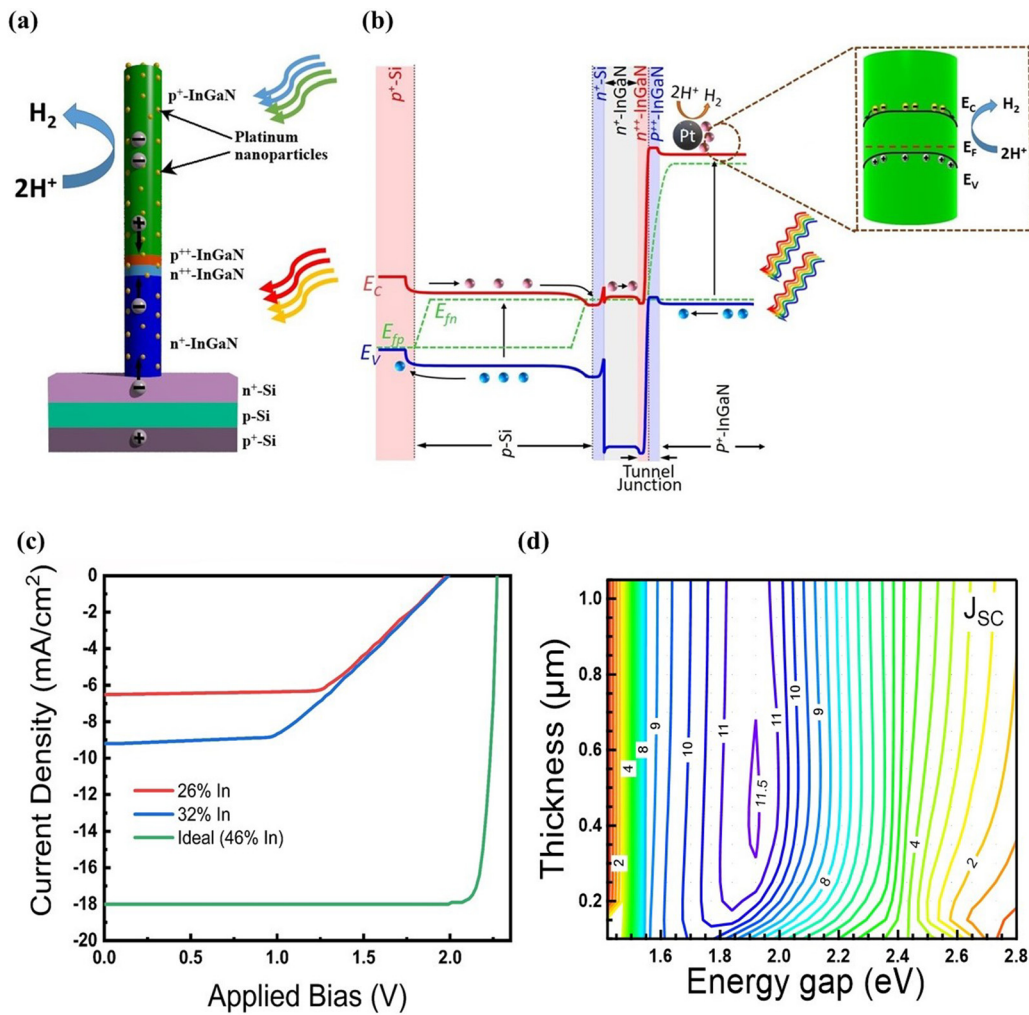
FIG. 1. (a) Schematic of Pt decorated p^+-InGaN/TJ/n^+-InGaN nanowire on n^+-p Si wafer.[34] (b) Energy band diagram under light illumination,[34] showing charge carrier generation in bottom Si and top p^+-InGaN and charge carrier (electron) extraction from p^+-InGaN for proton reduction reaction. Constant In composition has been assumed throughout the structure. The simulation input parameters are tabulated in supplementary material Table S1. (c) Theoretically calculated J–V curves of p^+-InGaN/TJ/n^+-InGaN/n^+-p Si photocathode at different indium compositions. The simulation input parameters of defects are tabulated in supplementary material Table S2. (d) Top p^+-InGaN thickness and energy gap dependence of the short circuit current density. Note that the input simulation parameters are shown in supplementary material Table S1.

photocathodes with different indium compositions are listed in Table I.

It is noticed that there is a large variation of indium composition in InGaN nanowire arrays based on previous studies,[28,34,43] leading to enhanced light absorption than what is possible for $In_{0.32}Ga_{0.68}N$ layers with uniform indium distribution. Our studies also showed that the device performance, including photocurrent density and onset potential, depends critically on p-type dopant incorporation (to be described next). Gas chromatograph (GC, Shimadzu GC-8A) equipped with a thermal conducting detector (TCD) was used for the detection of H_2. Figure 3(b) depicts the average experimental H_2 evolution (blue dots) at 0.6 V vs RHE under AM 1.5G one-sun illumination for 2 h. The calculated H_2 production (black dots) is also shown in the same plot. Faraday efficiency was evaluated from the H_2

evolution of the platinized p^+-InGaN/TJ/n^+-InGaN nanowires/n^+-p Si photocathode based on the following equation:

$$\eta_{Faraday}(\%) = \frac{2 \times n_{H2}(t = T_0)\,(\text{mol}) \times F}{\int_0^{T_0} I\,(\text{A}).dt\,(\text{s})} \times 100. \quad (1)$$

Here, $\eta_{Faraday}$ is the Faraday efficiency, I represents the measured photocurrent, F is the Faradaic constant (96 485 C/mol), and n_{H2} is the total H_2 production in T_0 time duration. The Faraday efficiency was calculated to be approximately 100% by correlating the measured and calculated H_2 evolution.
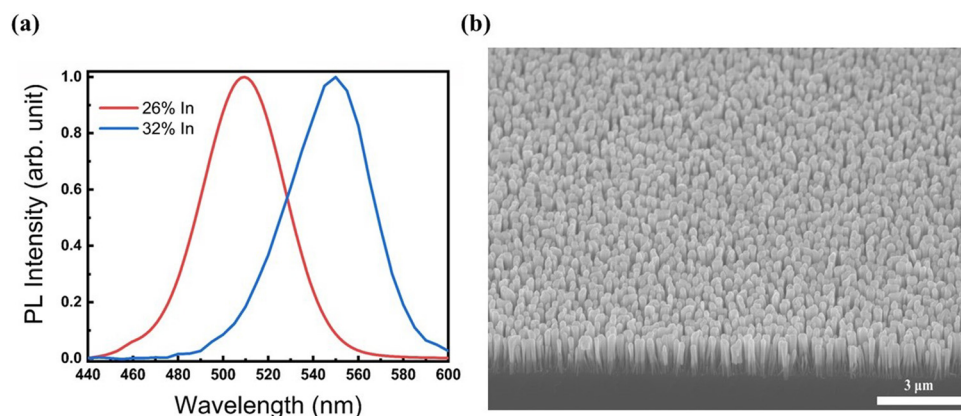
FIG. 2. (a) Normalized photoluminescence (PL) spectra at room temperature for p^+-InGaN/TJ/n^+-InGaN nanowires/n^+-p Si with two different indium compositions.[34] (b) SEM image of as-grown p^+-InGaN/TJ/n^+-InGaN nanowires on Si wafer.

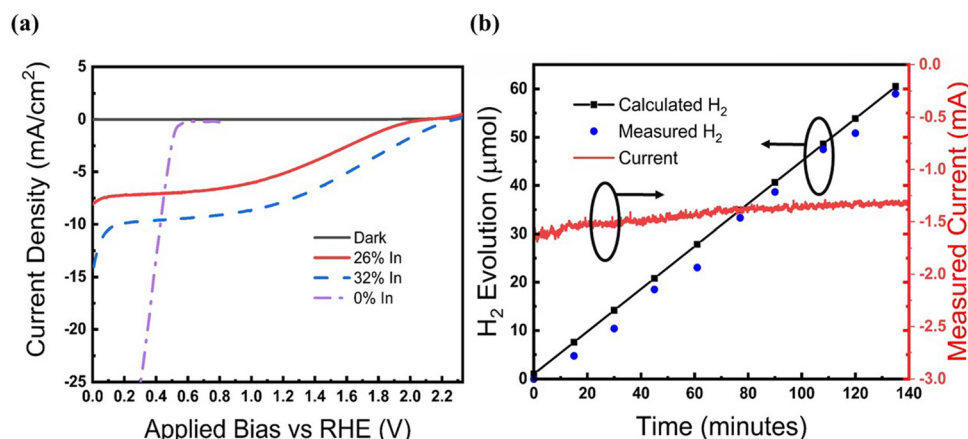**FIG. 3.** (a) Three-electrode linear scan voltammogram (LSV) measurements of p^+-InGaN/TJ/n^+-InGaN nanowires/n^+-p Si photocathode with different indium compositions [0%, 26%, and 32% (Ref. 34)] in 0.5 M H_2SO_4 under AM 1.5G one sun illumination and dark condition. The LSV scan of a single-junction GaN/Si photocathode is also shown for comparison. (b) H_2 production for p^+-InGaN/TJ/n^+-InGaN nanowires/n^+-p Si photocathode at 0.6 V vs RHE under AM 1.5G one-sun illumination in 0.5 M H_2SO_4.

Essential for the operation of InGaN/Si nanowire double-junction photocathode is the efficient charge carrier separation, collection, and extraction. In this regard, we have examined the role of Mg-dopant incorporation on the PEC performance. Figure 4(a) shows the three-electrode LSV of Pt/p^+-InGaN/TJ/n^+-InGaN nanowires/n^+-p Si photocathodes with an average indium composition ~26% for the top junction. The average p-type doping levels were estimated to vary from ~2.5×10^{16} cm^{-3} to 2.5×10^{17} cm^{-3}. It is seen that the device performance depends critically on the p-type dopant incorporation. A very low level of photocurrent density was measured for the sample with a

TABLE I. ABPE comparison of photocathodes with different indium compositions.

Sample (indium composition)	ABPE
0%	7.6%
26%	6.2%
32%	9.5%

low p-type doping concentration of 2.5×10^{16} cm^{-3}. Significantly increased photocurrent density was measured with increasing p-type doping to an optimum level (~1×10^{17} cm^{-3}). A drop in the photocurrent density was measured with further increasing the p-type doping concentration to ~2.5×10^{17} cm^{-3}. ABPE values of these photocathodes are presented in Table II. Similar trend of photocurrent density variation with respect to the p-type doping of the top p-InGaN was also observed for single-junction InGaN photocathodes. Our studies have also shown that the doping concentration in the tunnel junction, particularly Mg doping, plays a critical role on the device performance (supplementary material Fig. S2). At the optimum p-type doping level (estimated hole concentration ~5.5×10^{17} cm^{-3} in the tunnel junction), the photocurrent density value reaches a maximum value. Furthermore, increasing the doping concentration resulted in a decrease in the photocurrent density. Higher Mg concentration at the tunnel junction beyond the optimum level causes the creation of defect states, which makes the device more resistive resulting in the drop of photocurrent density.[44]
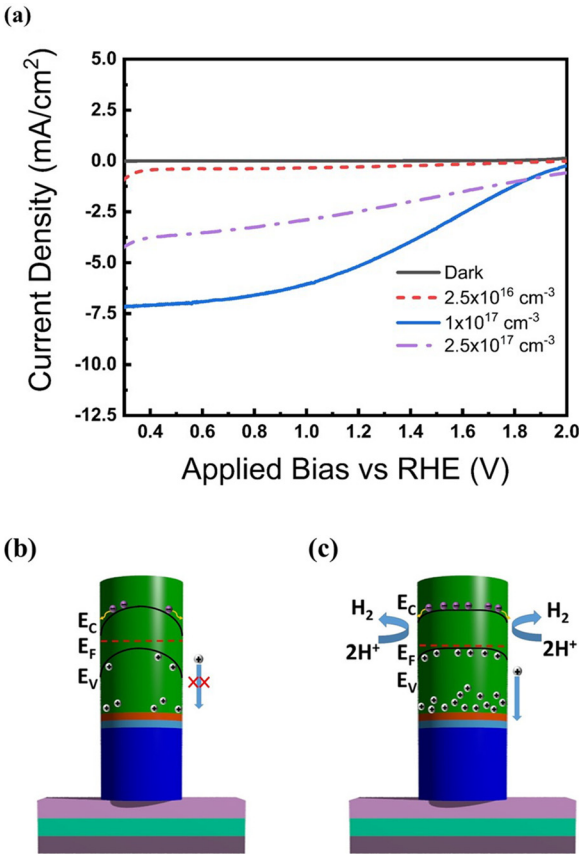
FIG. 4. (a) Three-electrode linear scan voltammogram (LSV) curves of p^+-InGaN/TJ/n^+-InGaN/n^+-p Si photocathode with different Mg concentrations in the top p-InGaN layer in 0.5 M H_2SO_4 under AM 1.5G one sun illumination and dark conditions. (b) Schematic of the energy band diagram for low Mg doping resulting in severe downward band bending with depleted vertical channel. (c) Schematic of the band diagram for optimum Mg doping with downward band bending and efficient vertical transport of photogenerated holes.

The underlying mechanisms for the critical role of Mg-dopant incorporation are discussed. Schematically illustrated in Figs. 4(b) and 4(c) are the charge carrier generation, extraction, and transport processes of the top InGaN junction. With relatively low Mg dopant incorporation, there is more depletion in the nanowire bulk and severe downward band bending because the surface is likely weakly n-type due to the surface desorption of Mg dopant,[45,46] shown in Fig. 4(b). The resulting bulk depletion, together with the large resistance

TABLE II. ABPE comparison of photocathodes with different Mg doping concentrations.

Sample (p-type doping concentration, cm^{-3})	ABPE
2.5×10^{16}	0.4%
1×10^{17}	6.2%
2.5×10^{17}	3.0%

associated with low Mg doping, significantly compromises, or even depletes the conduction channel for the vertical transport of photogenerated holes toward the tunnel junction.[47] Moreover, there will be more holes recombining at the nanowire surface/electrolyte interface owing to the inefficient vertical transport of photogenerated holes to the tunnel junction. Consequently, a very low level of photocurrent density was measured. With increasing Mg incorporation, the surface is transformed to be p-type and hence the surface band bending can be tuned by varying Mg-dopant incorporation. This makes it possible to optimize the device performance by controlling the p-type doping levels. At an optimum p-type doping level, the efficient vertical transport of photogenerated holes toward the tunnel junction is made possible, while maintaining sufficient downward surface band bending to allow efficient electron extraction along the nanowire lateral dimension for proton reduction reaction. Quantitative lateral band bending variation with respect to Mg doping level has also been depicted in Fig. S3 of the supplementary material. However, this modeling is based on the ideal case with the assumption that Mg doping is uniform across the nanowire lateral dimension and, as such, only the Fermi level difference between the InGaN nanowire and the electrolyte in the interface was taken into consideration for the nanowire surface band bending.

We have further calculated the J–V curves of $In_{0.26}Ga_{0.74}N$/Si photocathodes with various p-type doping concentrations in the top junction, shown in Fig. 5. It is seen that the short circuit current, J_{sc} increases substantially with increasing hole density from $\sim 2.5 \times 10^{16}$ cm^{-3} to 1×10^{17} cm^{-3}. A maximum photocurrent density ~ 7.4 mA/cm^2 was calculated for a hole concentration of $\sim 1 \times 10^{17}$ cm^{-3}. With further increasing doping concentration, a reduction of photocurrent density was observed. These general trends are in good agreement with experiments.

The theoretically calculated J–V curves of the photocathodes for different defect concentrations in the top junction, contact barrier height, series resistance, and shunt resistance were further studied (see Fig. S4 in the supplementary material). Increasing the defect concentrations gradually decreases the short current density without significantly affecting the onset voltage. On the other hand, the increase in contact barrier reduces the onset potential without affecting the current density values. The increase in series resistance adversely affects the fill factor, whereas low value of shunt resistance degrades all these performance parameters, i.e., fill factor, onset potential, as well as current density. The increase in Mg doping concentration gradually increases the layer defect concentration and affects the series and shunt resistance values. The impact of these non-ideality factors coupled with the optimum band bending effect has yielded an optimum p-type doping level of 1×10^{17} cm^{-3}, which agrees with experiment, as shown in Fig. 4(a).

The impact of surface recombination velocity on the device performance with ideal series and shunt resistance values was also taken into consideration (see Fig. S5 in the supplementary material). With increasing doping concentration, surface recombination increases. With low Mg doping, even though the surface recombination velocity remains relatively low, the carrier depletion results in low current density values. At an optimized doping level of 1×10^{17} cm^{-3}, better device performance is observed due to the efficient vertical transport of photogenerated holes as well as optimized surface band bending. Beyond this level of doping, the adverse impact of surface
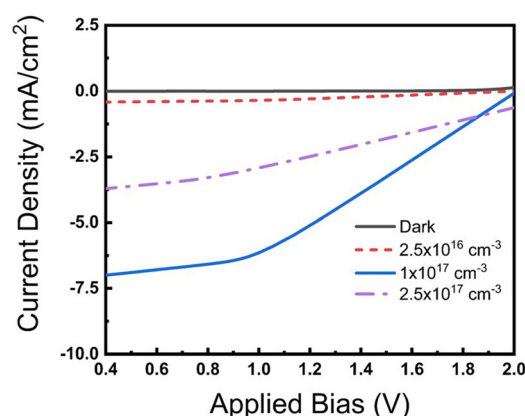
FIG. 5. Theoretically calculated J–V curves of p^+-InGaN/TJ/n^+-InGaN nanowires/n^+-p Si photocathode with different top p-InGaN layer Mg concentrations. Simulation input parameters can be found in supplementary material Table S3.

recombination velocity becomes more dominant and thus the device performance degrades, as shown in Figs. 4(a) and S5. Deeper surface defect energy, higher surface recombination velocity, and surface defect density jointly lead to enhanced surface defect states, which originate from high Mg doping beyond the optimum level in our tandem device. From Fig. S6 in the supplementary material, it can also be observed that increase in all three of these factors yields degraded device performance.

In summary, we have performed a combined theoretical and experimental study of the design and PEC performance of a p^+-InGaN/Si double-junction photocathode, including the effect of indium composition and Mg doping. Increasing indium composition has shown to significantly improve the photocurrent density due to the efficient solar photon absorption. The sample with 32% indium composition showed a maximum photocurrent density of $\sim$9 mA/cm^2 at 0.4 V vs RHE with ABPE of $\sim$9.5%. The critical role of p-type doping in the top InGaN junction is also identified, including the downward surface band bending for efficient extraction of photogenerated electrons for proton reduction and the creation of a vertical conduction channel along the nanowire dimension for the transport of photogenerated holes to the tunnel junction. An optimum p-type doping level $\sim$1 × 10^{17}cm^{-3} was identified both experimentally and theoretically. However, several challenges in material growth, such as epitaxy of defect-free In-rich InGaN, elimination of surface defects, and uniform Mg doping across the photocathode, remain to be addressed to further improve the device performance. Overall, these studies offer important insights for the development of high efficiency artificial photosynthesis devices for efficient and economical H$_2$ fuel production.

See the supplementary material for graphs of some additional experiments as well as simulations and parameters used for theoretical calculations.

AUTHORS' CONTRIBUTIONS

I.A.N. and S.V. equally contributed to this work.

DATA AVAILABILITY

The data that support the findings of this study are available from the corresponding author upon reasonable request.

REFERENCES

[1] A. Fujishima and K. Honda, "Electrochemical photolysis of water at a semiconductor electrode," Nature **238**, 37–38 (1972).
[2] B. AlOtaibi, M. Harati, S. Fan et al., "High efficiency photoelectrochemical water splitting and hydrogen generation using GaN nanowire photoelectrode," Nanotechnoloy **24**, 175401 (2013).
[3] H. Cui, W. Zhao, C. Yang et al., "Black TiO$_2$ nanotube arrays for high-efficiency photoelectrochemical water-splitting," J. Mater. Chem. A **2**, 8612–8616 (2014).
[4] Z. Dong, D. Ding, T. Li et al., "Black Si-doped TiO$_2$ nanotube photoanode for high-efficiency photoelectrochemical water splitting," RSC Adv. **8**, 5652 (2018).
[5] M. S. Prévot and K. Sivula, "Photoelectrochemical tandem cells for solar water splitting," J. Phys. Chem. C **117**, 17879–17893 (2013).
[6] L. C. Seitz, Z. Chen, A. J. Forman et al., "Modeling practical performance limits of photoelectrochemical water splitting based on the current state of materials research," ChemSusChem **7**, 1372–1385 (2014).
[7] S. Chu, W. Li, Y. Yan et al., "Roadmap on solar water splitting: Current status and future prospects," Nano Futures **1**, 022001 (2017).
[8] K. T. Fountaine, H. J. Lewerenz, H. A. Atwater et al., "Efficiency limits for photoelectrochemical water-splitting," Nat. Commun. **7**, 13706 (2016).
[9] J. L. Young, M. A. Steiner, H. Döscher et al., "Direct solar-to-hydrogen conversion via inverted metamorphic multi-junction semiconductor architectures," Nat. Energy **2**, 17028 (2017).
[10] O. Khaselev and J. A. Turner, "A monolithic photovoltaic-photoelectrochemical device for hydrogen production via water splitting," Science **280**, 425 (1998).
[11] Y. Wang, J. Schwartz, J. Gim et al., "Stable unassisted solar water splitting on semiconductor photocathodes protected by multifunctional GaN nanostructures," ACS Energy Lett. **4**, 1541–1548 (2019).
[12] S. Fan, I. Shih, and Z. Mi, "A monolithically integrated InGaN nanowire/Si tandem photoanode approaching the ideal bandgap configuration of 1.75/1.13 eV," Adv. Energy Mater. **7**(2), 1600952 (2016).
[13] F. W. Ostermayer and P. A. Kohl, "Photoelectrochemical etching of p-GaAs," Appl. Phys. Lett. **39**, 76–78 (1981).
[14] F. Nandjou and S. Haussener, "Degradation in photoelectrochemical devices: Review with an illustrative case study," J. Phys. D **50**, 124002 (2017).
[15] B. A. Pinaud, J. D. Benck, L. C. Seitz et al., "Technical and economic feasibility of centralized facilities for solar hydrogen production via photocatalysis and photoelectrochemistry," Energy Environ. Sci. **6**, 1983 (2013).
[16] R. T. Elafandy, M. Ebaid, J.-W. Min et al., "Flexible InGaN nanowire membranes for enhanced solar water splitting," Opt. Express **26**, A640 (2018).
[17] P. Varadhan, H.-C. Fu, D. Priante et al., "Surface passivation of GaN nanowires for enhanced photoelectrochemical water-splitting," Nano Lett. **17**, 1520 (2017).
[18] M. César, Y. Ke, W. Ji et al., "Band gap of In$_x$Ga$_{1-x}$N: A first principles analysis," Appl. Phys. Lett. **98**, 202107 (2011).
[19] S. Vanka, E. Arca, S. Cheng et al., "High efficiency Si photocathode protected by multifunctional GaN nanostructures," Nano Lett. **18**, 6530–6537 (2018).
[20] D. Bae, B. Seger, P. C. K. Vesborg et al., "Strategies for stable water splitting via protected photoelectrodes," Chem. Soc. Rev. **46**, 1933 (2017).
[21] B. AlOtaibi, H. P. T. Nguyen, S. Zhao, M. G. Kibria, S. Fan, and Z. Mi, "Highly stable photoelectrochemical water splitting and hydrogen generation using a double-band InGaN/GaN core/shell nanowire photoanode," Nano Lett. **13**(9), 4356–4361 (2013).

[22]R. Fan, W. Dong, L. Fang et al., "More than 10% efficiency and one-week stability of Si photocathodes for water splitting by manipulating the loading of the Pt catalyst and TiO_2 protective layer," J. Mater. Chem. A **5**, 18744 (2017).

[23]S. Vanka, K. Sun, G. Zeng et al., "Long-term stability studies of a semiconductor photoelectrode in three-electrode configuration," J. Mater. Chem. A **7**, 27612 (2019).

[24]A. Hussain, S. M. Arif, M. Aslam et al., "Emerging renewable and sustainable energy technologies: State of the art," Renewable Sustainable Energy Rev. **71**, 12–28 (2017).

[25]S. Arafin, X. Liu, and Z. Mi, "Review of recent progress of III-nitride nanowire lasers," J. Nanophotonics **7**, 074599 (2013).

[26]S. Fan, B. AlOtaibi, S. Y. Woo et al., "High efficiency solar-to-hydrogen conversion on a monolithically integrated InGaN/GaN/Si adaptive tunnel junction photocathode," Nano Lett. **15**, 2721–2726 (2015).

[27]M. Gopalakrishnan, S. Gopalakrishnan, G. M. Bhalerao, and K. Jeganathan, "Multiband InGaN nanowires with enhanced visible photon absorption for efficient photoelectrochemical water splitting," J. Power Sources **337**, 130–136 (2017).

[28]Y. Wang, S. Vanka, J. Gim et al., "An $In_{0.42}Ga_{0.58}N$ tunnel junction nanowire photocathode monolithically integrated on a nonplanar Si wafer," Nano Energy **57**, 405–413 (2019).

[29]M. G. Kibria, R. Qiao, W. Yang et al., "Atomic-scale origin of long-term stability and high performance of p-GaN nanowire arrays for photocatalytic overall pure water splitting," Adv. Mater. **28**, 8388–8397 (2016).

[30]S. Chu, S. Vanka, Y. Wang et al., "Solar water oxidation by an InGaN nanowire photoanode with a bandgap of 1.7 eV," ACS Energy Lett. **3**, 307–314 (2018).

[31]X. Guan, F. A. Chowdhury, Y. Wang et al., "Making of an industry-friendly artificial photosynthesis device," ACS Energy Lett. **3**(9), 2230–2231 (2018).

[32]T. D. Moustakas, "The role of extended defects on the performance of optoelectronic devices in nitride semiconductors," Phys. Status Solidi A **210**, 169–174 (2013).

[33]G. Zeng, T. A. Pham, S. Vanka et al., "Development of a photoelectrochemically self-improving Si/GaN photocathode for efficient and durable H_2 production," Nat. Mater. (published online 2021).

[34]S. Vanka, B. Zhou, R. A. Awni et al., "InGaN/Si double-junction photocathode for unassisted solar water splitting," ACS Energy Lett. **5**, 3741–3751 (2020).

[35]S. Krishnamoorthy, D. N. Nath, F. Akyol et al., "Polarization-engineered GaN/InGaN/GaN tunnel diodes," Appl. Phys. Lett. **97**, 203502 (2010).

[36]S. M. Sadaf, Y. H. Ra, T. Szkopek, and Z. Mi, "Monolithically integrated metal/semiconductor tunnel junction nanowire light-emitting diodes," Nano Lett. **16**, 1076–1080 (2016).

[37]S. M. Sadaf, Y.-H. Ra, H. P. T. Nguyen et al., "Alternating-current InGaN/GaN tunnel junction nanowire white-light emitting diodes," Nano Lett. **15**, 6696–6701 (2015).

[38]S. M. Sadaf, S. Zhao, Y. Wu et al., "An AlGaN core–shell tunnel junction nanowire light-emitting diode operating in the ultraviolet-C band," Nano Lett. **17**, 1212–1218 (2017).

[39]Y. Wang, Y. Wu, J. Schwartz et al., "A single-junction cathodic approach for stable unassisted solar water splitting," Joule **3**, 2444–2456 (2019).

[40]R. Cheriton, S. Sadaf, and Z. Mi, "InGaN/GaN quantum dots in nanowires on silicon (111) for intermediate band solar cells (WCPEC-7)," presented at the IEEE 7th World Conference on Photovoltaic Energy Conversion (WCPEC), Waikoloa, HI, 2018.

[41]B. Zhou, P. Ou, R. T. Rashid et al., "Few-atomic-layers iron for hydrogen evolution from water by photoelectrocatalysis," iScience **23**, 101613 (2020).

[42]B. AlOtaibi, X. Kong, S. Vanka et al., "Photochemical carbon dioxide reduction on Mg-doped Ga(In)N nanowire arrays under visible light irradiation," ACS Energy Lett. **1**, 246–252 (2016).

[43]S. Fan, S. Y. Woo, S. Vanka, G. A. Botton, and Z. Mi, "An $In_{0.5}Ga_{0.5}N$ nanowire photoanode for harvesting deep visible light photons," APL Mater. **4**(7), 076106 (2016).

[44]M. P. Ulmer, B. W. Wissels, B. Han et al., "Advances in wide-bandgap semiconductor based photocathode devices for low light level applications," Proc. SPIE **5164**, 144–154 (2003).

[45]M. G. Kibria, F. A. Chowdhury, S. Zhao et al., "Visible light-driven efficient overall water splitting using p-type metal-nitride nanowire arrays," Nat. Commun. **6**, 6797 (2015).

[46]M. G. Kibria, S. Zhao, F. A. Chowdhury et al., "Tuning the surface Fermi level on p-type gallium nitride nanowires for efficient overall water splitting," Nat. Commun. **5**, 3825 (2014).

[47]P. Mondal, B. Ghosh, P. Bal et al., "Planar junctionless transistor with non-uniform channel doping," Appl. Phys. Lett. **102**, 133505 (2013).